Jurnal Kejuruteraan 38(7) 2026: 3673-3682
https://doi.org/10.17576/jkukm-2026-38(7)-38

Structural and Morphological Characterization of Bifunctional ZnCoS/NF Catalysts Synthesized Under Varying Conditions for Potential Electrocatalytic Applications

Nor Atikah Abu Bakar, Kee Shyuan Loh*, Kean Long Lim, Wai Yin Wong & Rozan Mohamad Yunus

Fuel Cell Institute, Universiti Kebangsaan Malaysia, 43000, Bandar Baru Bangi, Selangor, Malaysia

**Corresponding author: ksloh@ukm.edu.my*

Received 24 December 2025, Received in revised form 2 June 2026
Accepted 2 July 2026, Available online 30 October 2026

ABSTRACT

Growing concerns over global air pollution have intensified interest in hydrogen as a clean and sustainable energy carrier capable of generating both heat and electricity. Developing efficient and cost-effective electrocatalysts is essential for improving the sluggish hydrogen and oxygen evolution reactions in alkaline water electrolysis. In this study, CoS and Zn-doped CoS (ZnCoS) catalysts were synthesized on nickel foam (NF) using a two-step hydrothermal method, with systematic variations in Zn:Co molar ratios and synthesis temperatures. Structural and morphological characterisation revealed that incorporating Zn^{2+} into CoS significantly modified the catalyst architecture, transforming the moss-like CoS morphology into well-defined flower-like nanostructures composed of interconnected nanoflakes. These nanostructures enhanced surface roughness and porosity, providing greater accessibility to electrochemically active sites. XRD and HRTEM analyses further confirmed the successful incorporation of Zn into the CoS lattice through observable lattice distortion and the coexistence of CoS_2 and $Zn_{0.76}Co_{0.24}S$ phases. Among the synthesized samples, ZnCoS prepared at a 1:3 Zn:Co ratio and 100 °C exhibited the smallest crystallite size, lowest cell volume, and the most favourable nanoflake assembly. In contrast, higher synthesis temperatures led to increased crystallite growth and reduced porosity. Overall, this study establishes a clear structure–morphology relationship and identifies ZnCoS/NF prepared at low synthesis temperatures as a promising candidate for further electrochemical evaluation toward alkaline water electrolysis applications.

Keywords: Catalysts; ZnCoS; characterization; structural and morphological; alkaline water electrolysis

INTRODUCTION

The growing concern over global air pollution in recent years has intensified interest in hydrogen as a clean and sustainable energy source. Hydrogen is a versatile energy carrier that can be utilised to generate both electricity and heat across a wide range of applications (Faid et al. 2021). Consequently, the term "hydrogen economy" has emerged to describe the pivotal role of hydrogen in future energy technologies. The production of green hydrogen is primarily achieved through water electrolysis (Ferriday et al. 2023). Currently, three major types of water electrolysers are widely recognised: alkaline water electrolyser (AWE), polymer electrolyte membrane water electrolyser (PEMWE), and anion exchange membrane water electrolyser (AEMWE) (Morais et al. 2023).

Water electrolysis is an electrochemical process that uses electricity to split water into hydrogen (H_2) and oxygen (O_2) gases. The AEMWE system combines the advantages of AWE and PEMWE by utilising alkaline water and a polymeric membrane as the electrolyte and electrode separator, respectively (Wu et al. 2023). However, unlike AWE, AEMWE operates with a low-concentration alkaline electrolyte, and the polymeric membrane facilitates anion (OH^-) rather than cation (H^+) transport. Another crucial factor in AEMWE performance is the electrocatalyst used at the anode and cathode. These catalysts must exhibit high oxygen evolution reaction (OER) and hydrogen evolution reaction (HER) kinetics, as well as excellent stability in alkaline media (Viteri et al. 2023). AEMWE technology enables the substitution of expensive noble metals with transition-metal-based materials, offering a cost-effective yet high-performance alternative. Effective electrocatalysts must demonstrate high electrocatalytic activity, strong

corrosion resistance in alkaline environments, low electrical resistance, high selectivity, and good stability under intermittent power conditions, while remaining economically viable (Sugawara et al. 2023). One of the principal advantages of alkaline electrolysis over its acidic counterpart is the stability of non-precious metals. Although platinum-group metals (PGMs) display excellent performance due to their low overpotentials, their high cost limits large-scale application (Silva et al. 2023). As a result, extensive research has focused on developing earth-abundant transition-metal catalysts. Among these, nickel (Ni) has emerged as a promising material due to its corrosion resistance, low cost, and suitability as both an active catalyst and conductive substrate in alkaline electrolysis (Wang et al. 2023). In particular, nickel foam (NF) provides a three-dimensional conductive network, making it an ideal substrate for catalyst growth. Catalysts play a central role in determining AEMWE efficiency. Various strategies have been explored to enhance catalytic performance, including carbon composite formation, defect engineering, thickness reduction, heteroatom doping, morphology regulation, particle size control, heterostructure synthesis, phase variation, and single-atom catalyst (SAC) design (Krishnamachari et al. 2025). Nevertheless, the performance of these catalysts still lags behind that of noble metals such as platinum (Pt), prompting ongoing efforts to identify efficient, low-cost alternatives. Zinc (Zn) and cobalt (Co) have been recognised as promising candidates due to their synergistic chemical and electronic properties. Zn contributes to the structural stability of the catalyst, while Co plays a key role in redox reactions, facilitating charge transfer during both OER and HER processes through its multiple oxidation states. When combined with sulfides, the resulting materials exhibit enhanced electrical conductivity and excellent catalytic durability in alkaline media.

Therefore, in this study, we investigate the morphological and structural characteristics of ZnCoS catalysts synthesized on nickel foam under different Zn:Co molar ratios and synthesis temperatures. The aim is to identify the optimal synthesis conditions that yield superior catalyst morphology and structure for potential AEMWE applications. The performance of catalysts in AEMWE is strongly influenced by their structural and morphological properties, making FESEM, HRTEM and XRD essential characterization tools for understanding and optimizing catalytic behaviour. The FESEM and HRTEM provide detailed visualization of surface morphology, including particle size, porosity, nanosheet formation, or hierarchical architectures, all of which directly influence the electrochemically active surface area (ECSA), gas-bubble release, and overall mass transport which are critical factors for achieving high current densities in AEMWE. Meanwhile, HRTEM and XRD reveal the crystalline phases, purity, and degree of crystallinity present in the catalysts, offering insights into intrinsic electronic conductivity, phase stability, and the tendency of materials to undergo structural reconstruction under operating conditions. Together, FESEM, HRTEM and XRD enable the establishment of a comprehensive structure–performance relationship, facilitating the design of catalysts that combine high accessibility of active sites with stable, conductive phases suitable for long-term alkaline electrolys

METHODOLOGY

MATERIALS

Cobalt nitrate hexahydrate ($(CoNO_3)_2 \cdot 6H_2O$, Sigma Aldrich), zinc nitrate hexahydrate ($(ZnNO_3)_2 \cdot 6H_2O$, Sigma Aldrich), sodium sulfide (Na_2S, Chemiz), urea (Chemiz), ethanol (Merck), nickel (Ni) foam (Good Fellow), potassium hydroxide (KOH), hydrochloric acid (HCl), deionized (DI) water, and commercial electrodes, namely NiFeCo/Ni mesh and $NiFe_2O_4$/C, both obtain from Dioxide Materials were used in this study.

SYNTHESIS OF CoS/NF AND ZnCoS/NF

A piece of Ni foam was cut into 1 × 2 cm² and used as the substrate. The Ni foam was sonicated in 0.5 M HCl solution for 10 minutes at a frequency of 50 kHz to remove surface oxides. It was then rinsed three times with ethanol and DI water using a sonicator (10 minutes each, 50 kHz) to eliminate any residual acid. After cleaning, the substrate was dried in an oven at 60 °C overnight.

Different Zn:Co molar ratios, namely 0.25:0.75, 0.50:0.50, 0.75:0.25, and 0:1, were prepared and denoted as 1:3, 1:1, 3:1, and CoS, respectively. The corresponding samples were labelled as ZnCoS/NF_13, ZnCoS/NF_11, and ZnCoS/NF_31 for catalysts grown on nickel foam, and ZnCoS_13, ZnCoS_11, and ZnCoS_31 for the powder samples. The samples were prepared by stirring the respective metal precursors in 200 mL of deionised water until the solution turned pinkish or purplish, depending on the Co content. Urea was then added to the solution and stirred until homogeneous. The mixture was transferred into a 100 mL Teflon-lined autoclave along with the pre-cleaned Ni foam. The autoclave was subjected to a hydrothermal reaction at different temperatures (100, 150, and 200 °C) for 5 hours in a furnace. After the reaction, the deposited ZnCo on Ni foam was washed three times with ethanol and DI water, then dried in an oven at 70 °C

overnight. Subsequently, the dried ZnCo/NF sample was immersed in 0.1 M Na_2S solution and placed in a Teflon-lined autoclave for sulfidation at the same synthesis temperatures (100, 150, and 200 °C) for 5 hours. The resulting ZnCoS/NF sample was washed three times with ethanol and DI water, followed by drying in an oven at 70 °C overnight.

PHYSICAL CHARACTERISATION

The surface morphology of bare Ni foam, synthesized CoS/NF, and ZnCoS/NF was examined using field emission scanning electron microscopy (FESEM, Carl Zeiss Merlin). Elemental composition and distribution were analyzed via energy-dispersive X-ray spectroscopy (EDX, Oxford Instruments). Structural changes of the samples were investigated using X-ray diffraction (XRD, Bruker AXS D8 Advance Diffractometer) within a 2θ range of 10°–90°.

ELECTROCHEMICAL CHARACTERISATION

Electrochemical evaluation of all samples was carried out in a three-electrode setup with a Potentiostat/Galvanostat Autolab instrument. A 1.0 M KOH solution was used as the electrolyte. The NiFeCo/Ni mesh commercial electrode for HER, NiFe2O4/C commercial electrode for OER, synthesized ZnCoS/NF_13 100 electrode, and bare nickel foam (NF) substrate were used as working electrodes. A platinum wire and Hg/HgO electrode were used as the counter and reference electrode, respectively. Linear sweep voltammetry (LSV) analysis was conducted at the scan rate of 5 mVs^{-1}. The overpotential values of all electrodes were calculated using this equation η = E vs. RHE - 1.23 V for the OER region and η = E vs. RHE - 0 V for the HER region. Furthermore, electrochemical impedance spectroscopy (EIS) measurements were performed over a frequency range of 0.1 Hz to 100 kHz with an amplitude of 10 mV. Only a of 1×1 cm^2 active area of each samples was immersed in the KOH solution.

RESULTS AND DISCUSSION

EFFECT OF DIFFERENT MOLAR RATIO ON STRUCTURAL AND MORPHOLOGICAL PROPERTIES

The as-received Ni foam (NF) was cut into 1 × 2 cm^2 pieces and washed with 0.5 M HCl, ethanol, and deionized (DI) water, then dried at 60 °C overnight prior to morphological analysis. Clear SEM images at different magnifications (500×, 10 000×, and 30 000×) of the bare NF show a smooth surface free from impurities, dirt, or grease. (Figure 1 (a1-a3)). In agreement with Bakar et al. (2022), the bare NF exhibits a three-dimensional (3D) network structure with several loose, sponge-like microporous features arranged in a crisscross pattern at lower magnifications. At higher magnification, the surface of the bare NF appears smooth, with a few small indentations attributed to manufacturing factors.

The morphology of CoS/NF at various magnifications (Figure 1 (b1-b3)) was examined after the hydrothermal and sulfidation processes. The FESEM images reveal a significant change: the smooth surface of the bare NF becomes roughened, displaying a moss-like CoS structure. At lower magnification (Figure 1 (b1)), all areas of the NF are observed to be fully covered with CoS, while at higher magnification the detailed morphology of the nanostructure becomes evident. (Figure 1 (b3)). The chemical reactions that occur during the hydrothermal synthesis are as follows (Li et al. 2025):

$$Co(NO_3)_2 \rightarrow Co^{2+} + 2NO_3^- \quad (1)$$

$$Co^{2+}(aq) + S^{2-}(aq) \rightarrow CoS(s) \quad (2)$$

$$Co(NO_3)_2(aq) + Na_2S(aq) \rightarrow CoS(s) + 2NaNO_3(aq) \quad (3)$$

The synthesized ZnCoS samples with different Zn:Co molar ratios are denoted as 0.25:0.75 (1:3), 0.5:0.5 (1:1), and 0.75:0.25 (3:1). The morphology of ZnCoS/NF_13 (Figure 1 (c1-c3)) at various magnifications reveals a uniform dispersion of ZnCoS_13 across the surface of NF, indicating that the initially smooth surface of the NF substrate becomes significantly roughened following the ZnCoS_13 growth. The FESEM images further confirm a noticeable increase in porosity, which is expected to enhance more ion transport during water electrolysis. At higher magnification, a distinct flower-like structure composed of interconnected nanoflakes of ZnCoS_13 can be clearly observed. The morphological characteristic is consistent with finding reported by Li et. al. (2025), in which *in situ* carbon-encapsulated $CoS_2/Zn_{0.76}Co_{0.24}S$ nanoparticles exhibit a three-dimensional (3D) spherical flower-like nanosheets structure with uniformly dispersed nanoparticles anchored on the surface.

Similarly, the morphology of ZnCoS/NF_11(Figure 1 (d1-d3) shows that, at lower magnification, ZnCoS_11 uniformly covers the pillars of the NF, while at higher magnification, flake-like structures become apparent. The FESEM images of ZnCoS/NF_31 at different magnifications in Figure 1 (e1-e3) reveal a uniform dispersion of ZnCoS_31 coating the NF surface (Figure 1 (e1)). At higher magnification, distinct flake-like morphologies can be seen, confirming that the smooth NF surface has been successfully roughened through ZnCoS_31 growth. The

EDX analysis in the Figure 1 (f) corresponding to ZnCoS/NF_13 shows the elemental mapping of Ni, Co, Zn, and S, confirming the uniform distribution of ZnCoS_13 across the NF surface.

The simplified chemical reactions involved in the hydrothermal growth of ZnCoS on NF are as follows:

Step 1: Dissociation of metal salt

$$Zn(NO_3)_2\ (aq) \rightarrow Zn^{2+}\ (aq) + 2NO_3^-\ (aq) \quad (4)$$

$$Co(NO_3)_2\ (aq) \rightarrow Co^{2+}\ (aq) + 2NO_3^-\ (aq) \quad (5)$$

Step 2: Urea hydrolysis

$$CO(NH_2)_2 + 3H_2O \rightarrow 2NH_4^+ + CO_3^{2-} + 2OH^- \quad (6)$$

Step 3: Formation of hydroxides

$$Zn^{2+} + Co^{2+} + 4OH^- + CO_3^{2-} \rightarrow Zn(OH)_2\ (s) + Co(OH)_2\ (s) \quad (7)$$

Step 4: Sulfidation

Dissociation of sodium sulfide:

$$Na_2S\ (aq) \rightarrow 2Na^+ + S^{2-} \quad (8)$$

Then, sulfurization

$$Zn(OH)_2\ (s) + Co(OH)_2\ (s) + S^{2-}\ (aq) \rightarrow ZnCoS + 4OH^- \quad (9)$$

Urea was employed as a slow OH^- releasing agent during hydrothermal reaction. Upon thermal decomposition, urea gradually generates OH^- and CO_3^{2-} ions, enabling controlled precipitation of Zn^{2+} and Co^{2+} species.

To examine the structural properties of the synthesized CoS and ZnCoS samples, X-ray diffraction (XRD) analysis was conducted. As shown in Figure 1 (g), the XRD patterns of NF, CoS, ZnCoS_13, ZnCoS_11, and ZnCoS_31 are presented. All samples, except for NF, were obtained in powder form, collected from the residues remaining in the Teflon-lined autoclave. The powder residues are expected to have similar physicochemical properties to the catalyst deposited on the NF, as both were obtained from the same autoclave reaction. This is supported by the FESEM observation of the catalyst grown on NF, which showed similar characteristics to the images of the powder catalyst collected from the residue. Due to limitation of X-ray analysis for the ZnCoS catalyst deposited on NF, the Ni signal from the substrate dominated and masked the Zn and Co signals. Therefore, the powder sample is more suitable for this characterisation method. The XRD pattern of CoS corresponds to the cattierite structure of CoS_2 (JCPDS No. 41-1471). The diffraction peaks observed at 26.7° and 34.0° are attributed to the (111) and (210) planes of cubic CoS, respectively. The cattierite structure is also evident in samples synthesized with different Zn/Co molar ratios. Increasing the Zn:Co ratio beyond 1:3 results in the formation of a mixed phase consisting of CoS and $Zn_{0.76}Co_{0.24}S$ (JCPDS No. 47-1656). Compared to the pure CoS sample, ZnCoS_13 displays additional diffraction peaks, indicating lattice distortion caused by the incorporation of Zn atoms into the Co interstitial sites. The appearance of these peaks can be attributed to the substitution of Zn^{2+} ions for Co^{2+} ions, as the ionic radius of Zn^{2+} (74 pm) is slightly smaller than that of Co^{2+} (74.5 pm) (Prabhakaran Shyma & Sellappan 2023). A similar trend is observed for ZnCoS_11, whereas a reduction in diffraction peak intensity is noted for ZnCoS_31.

High-resolution transmission electron microscopy (HRTEM) was performed on ZnCoS_13 and CoS to further investigate their morphologies. The HRTEM images (Figure 1 (h1) and (i1) clearly show that Zn^{2+} ions were successfully incorporated into the CoS lattice. The lattice fringe of ZnCoS_13, calculated using ImageJ software, exhibits a spacing of 0.318 nm corresponding to the (111) plane, which is slightly smaller than that of CoS (0.319 nm, (Figure 1 (i2)). These observations confirm that both samples are polycrystalline in nature. The selected area electron diffraction (SAED) patterns (Figure 1 (h3) and (i3)) display multiple concentric rings with varying radii, further confirming the polycrystalline character of the synthesized samples. The diffraction rings in the SAED pattern of ZnCoS_13 correspond to the (111), (200), and (220) crystal planes, while those in CoS correspond to the (111) and (210) planes. The identified *hkl* planes are consistent with the XRD data, validating the polycrystalline nature of both ZnCoS_13 and CoS samples.

The average crystallite sizes of the synthesized samples, as summarized in Table 1, were found to be 40.70, 23.03, 46.48, and 62.71 nm for CoS, ZnCoS_13, ZnCoS_11, and ZnCoS_31, respectively. The Scherrer equation (Equation 8) was employed to calculate the average crystallite size of the prepared samples (Arumugam et al. 2025).

$$D = \frac{0.9\,\lambda}{B\cos\theta} \quad (8)$$

The lattice parameters of the prepared samples were calculated using Equation 9 (Bibi et al. 2025):

$$\frac{1}{d^2\,hkl} = \frac{4}{3}\left(\frac{h^2+hk+k^2}{a^2}\right) + \frac{l^2}{c^2} \quad (9)$$

The volume of the unit cell was calculated based on the cubic crystal system using Equation 10:

$$V = a \times b \times c \quad (10)$$

Table 1 summarizes the lattice characteristics of the prepared ZnCoS materials. The lattice parameters and unit cell volume exhibit a decreasing trend with increasing Zn^{2+} concentration, indicating the successful incorporation of Zn^{2+} ions into the CoS lattice. Notably, the lattice parameters of ZnCoS_11 and ZnCoS_31 are slightly lower than those of ZnCoS_13. This obversvation contrasts with the findings of Prabhakaran Shyma and Sellappan (2023), who reported an increase in lattice parameter and cell volume with a higher Zn ratio in ZnCoS. Although Zn^{2+} possesses a larger ionic radius than Co^{2+}, its stronger preference for tetrahedral coordination compared to Co^{2+}, which commonly occupies octahedral sites and can induce cation redistribution within the lattice. Such redistribution may lead to shorter average M–S bond distances, ultimately resulting in lattice contraction rather than expansion. This provides a plausible explanation for the trend observed in our samples. Therefore, these results suggest that a lower Zn^{2+} concentration (as in ZnCoS_13) promotes more effective incorporation of Zn^{2+} into the CoS crystal fram while preserving its structural characteristics, thereby facilitating the formation of a stable bimetallic Zn–Co–S phase, as further corroborated by the XRD analysis.

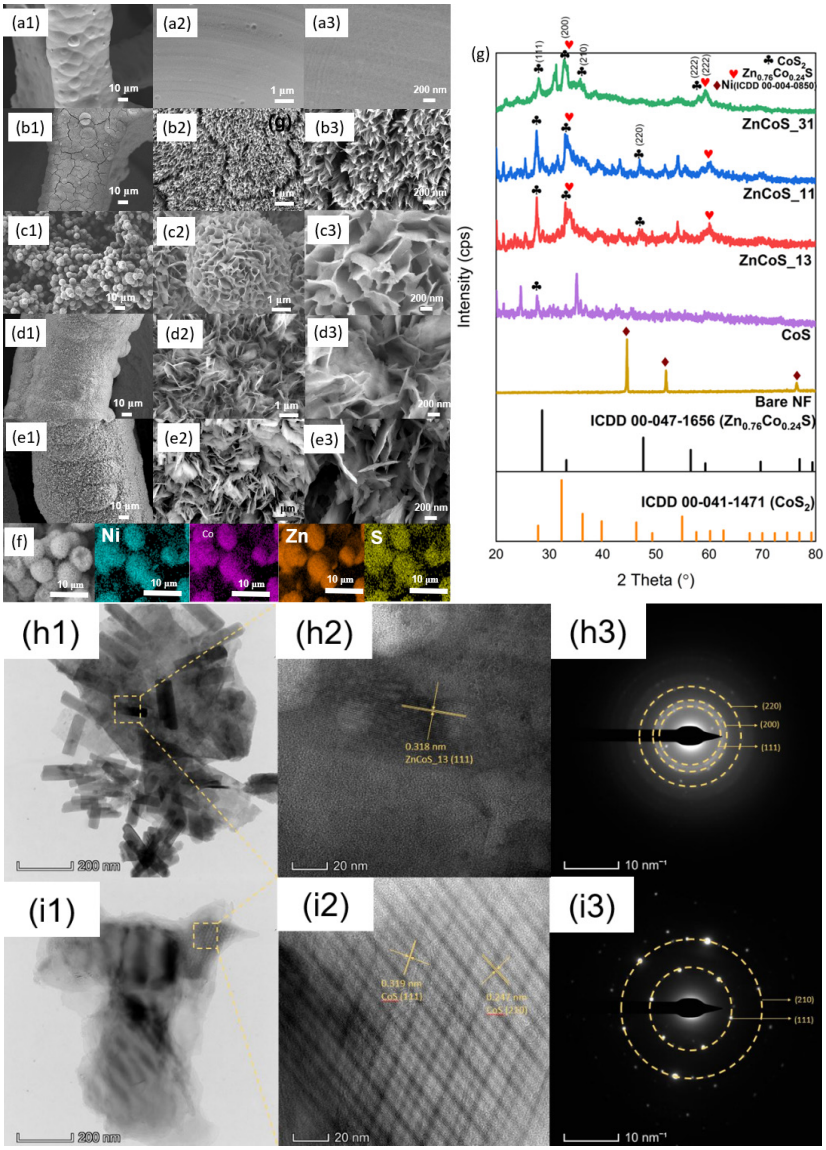


FIGURE 1. FESEM images at different magnifications — 500×, 10,000×, and 30,000× — for (a1–a3) bare NF, (b1–b3) CoS/NF, (c1–c3) ZnCoS/NF_13, (d1–d3) ZnCoS/NF_11, and (e1–e3) ZnCoS/NF_31; (f) EDX spectrum of ZnCoS/NF_13; (g) XRD patterns of bare NF, CoS, ZnCoS/NF_13, ZnCoS/NF_11, and ZnCoS/NF_31; HRTEM images of (h1) ZnCoS_13 and (i1) CoS; interlayer (d-spacing) measurements of (h2) ZnCoS_13 and (i2) CoS; and SAED patterns of (h3) ZnCoS_13 and (i3) CoS.

TABLE 1. Lattice parameters, unit cell volume, average crystallite size and crystallinity of CoS, ZnCoS_13, ZnCoS_11 and ZnCoS_31 calculated using Diffrac.eva software.

Molar ratio	Lattice parameter (Å) a=b=c	Unit Cell volume ($Å^3$)	Avg crystallite size. D (nm)	Crystallinity (%)
(0:1) CoS	5.54	170.03	40.70	62.3
(0.25:0.75) ZnCoS_13	5.48	164.57	23.03	47.0
(0.50:0.50) ZnCoS_11	5.42	159.22	46.48	45.8
(0.75:0.25) ZnCoS_31	5.39	156.59	62.71	31.9

EFFECT OF DIFFERENT SYNTHESIS TEMPERATURE ON THE STRUCTURAL AND MORPHOLOGICAL PROPERTIES

Based on the previous results, ZnCoS/NF_13 exhibited superior catalytic performance in terms of its structural and morphological characteristics. Therefore, this sample was selected to investigate the effect of different synthesis temperatures (100, 150, and 200 °C). The resulting samples are denoted as ZnCoS/NF_13-100, ZnCoS/NF_13-150, and ZnCoS/NF_13-200, corresponding to their synthesis temperatures. As shown in Figure 2 (a1-a3), he FESEM images of ZnCoS/NF_13-100 reveal a 3D spherical flower-like morphology composed of uniformly distributed, interconnected nanoflakes on the NF surface. With increasing synthesis temperature to 150 and 200 °C (Figure 2 (b1 and c1)), the size of the flower-like structures increased notably. At higher magnifications (Figure 2 (b2, b3, c2 and c3), the interconnected nanoflakes are seen to grow significantly larger (Li et al. 2025). This suggests an accelerated crystal growth rate, enhancing ZnCoS nucleation.

At elevated temperatures, Zn^{2+}, Co^{2+}, and S^{2-} ions exhibit higher mobility and energy, resulting in fewer but larger crystals rather than numerous smaller ones (Park et al. 2023). Additionally, the Ostwald ripening effect may contribute to this process, as higher temperatures promote the dissolution of smaller nanoparticles and the subsequent re-deposition of ions onto larger surfaces. The EDX analysis in the Figure 2 (d) corresponding to ZnCoS/NF_13-100 confirms the presence and uniform distribution of Ni, Co, Zn, and S elements within the synthesized sample.

To further examine the structural properties of samples synthesized at different temperatures, XRD characterization was performed. The XRD patterns of ZnCoS_13-100, ZnCoS_13-150, and ZnCoS_13-200 are shown in Figure 2 (e). To ensure data reliability, the XRD measurements were conducted on powder samples collected from residues after the hydrothermal process. The XRD spectra reveal the coexistence of cubic cattierite (CoS_2) (JCPDS No. 41-1471) and $Zn_{0.76}Co_{0.24}S$ (JCPDS No. 47-1656) phases. The HRTEM images in the Figure *2* (f1, g1 and h1) corresponding to ZnCoS_13-100, ZnCoS_13-150, and ZnCoS_13-200 show lattice spacings of 0.318, 0.274, and 0.197 nm, respectively. The SAED patterns (Figure 2 (f3), (g3) and (h3)) display multiple concentric rings with varying radii, confirming the polycrystalline nature of the synthesized samples. These lattice spacings correspond to the (111), (200), and (220) planes of CoS_2 and $Zn_{0.76}Co_{0.24}S$, consistent with the XRD results.

Table 2 highlights the lattice properties of the synthesized samples at different temperatures. The lattice parameters and unit cell volume increase significantly with increasing synthesis temperature. This trend is consistent with the FESEM images, where the size of the 3D spherical flower-like structures also increases. The average crystallite size shows a similar upward trend; however, as the crystallite size increases, the porosity of the synthesized samples decreases. The crystallinity of the samples also improves, as higher synthesis temperatures provide sufficient thermal energy for atoms to reorganize into a more ordered lattice structure. Nevertheless, for water electrolyser applications, maintaining adequate porosity is more crucial, as it plays a key role in ensuring efficient catalytic performance.

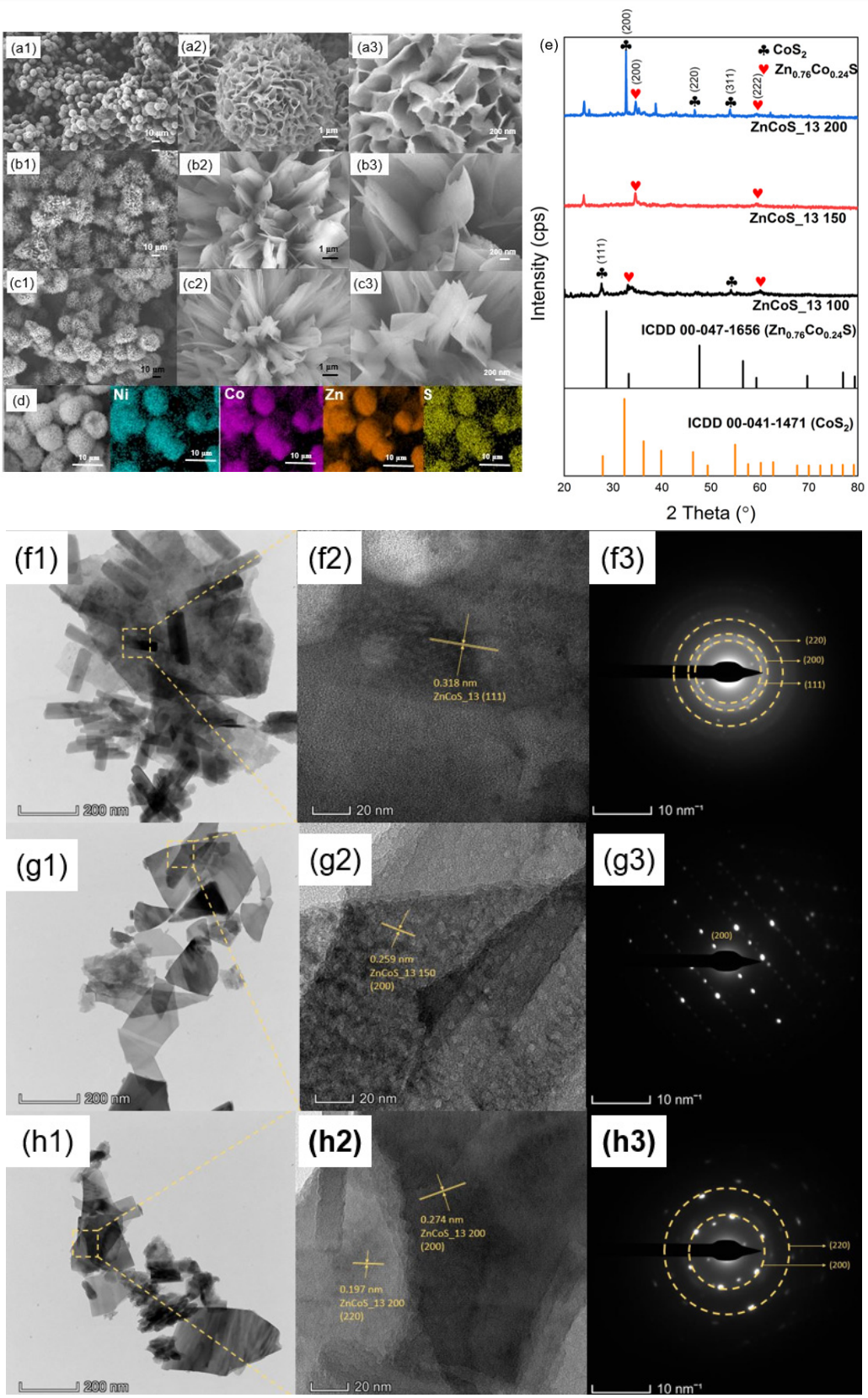


FIGURE 2. FESEM images at different magnifications — 500×, 10,000×, and 30,000× — for (a1–a3) ZnCoS/NF_13 100, (b1–b3) ZnCoS/NF_13 150, and (c1–c3) ZnCoS/NF_13 200; (d) EDX spectrum of ZnCoS/NF_13 100; (e) XRD patterns of ZnCoS/NF_13 100, ZnCoS/NF_13 150, and ZnCoS/NF_13 200; HRTEM images of (f1) ZnCoS_13 100, (g1) ZnCoS_13 150, and (h1) ZnCoS_13 200; interlayer (d-spacing) measurements for (f2) ZnCoS_13 100, (g2) ZnCoS_13 150, and (h2) ZnCoS_13 200; and SAED patterns of (f3) ZnCoS_13 100, (g3) ZnCoS_13 150, and (h3) ZnCoS_13 200.

TABLE 2. Lattice properties of the synthesized ZnCoS_13 100, ZnCoS_13 150, and ZnCoS_13 200 samples.

Sample Synthesis temperature (°C)	Lattice parameter a=b=c (Å)	Unit Cell volume (Å^3)	Avg crystallite size, D (nm)	Crystallinity (%)
ZnCoS_13 100	5.48	164.57	23.03	47.0
ZnCoS_13 150	5.53	169.11	33.26	48.5
ZnCoS_13 200	5.82	197.14	47.05	56.3

ELECTROCHEMICAL PERFORMANCE OF THE SYNTHESIZED CATALYST

The electrocatalytic performance of the prepared electrodes was evaluated using linear sweep voltammetry (LSV) and electrochemical impedance spectroscopy (EIS), as shown in Figure 3(a–f). The LSV curves reveal significant differences in catalytic activity among the investigated samples. For the hydrogen evolution reaction (HER), the NiFeCo/Ni mesh electrode exhibited the highest cathodic current density across the investigated potential range, indicating superior HER activity compared to ZnCoS/NF_13 100 and bare NF. At a given overpotential, the NiFeCo/Ni mesh generates substantially higher current densities, suggesting faster reaction kinetics and more efficient hydrogen production. The enhanced HER performance can be attributed to the synergistic interaction among Ni, Fe, and Co species, which optimizes the electronic structure of the catalyst and facilitates proton adsorption and hydrogen desorption processes. In contrast, bare NF exhibits the lowest current density, indicating its limited intrinsic catalytic activity toward HER.

The charge-transfer characteristics of the electrodes were further investigated using EIS measurements. The Nyquist plots in Figure 3(b) show that the NiFeCo/Ni mesh exhibited a small semicircle diameter among the HER catalysts, indicating low charge-transfer resistance and favourable HER kinetics. Conversely, bare NF showed the largest semicircle diameter, indicating poor charge-transfer capability and slower reaction kinetics. However, as tabulated in Table 3, the fitted R_{ct} value obtained showed that ZnCoS/NF_13 100 possessed the lowest charge-transfer resistance. Although the difference in R_{ct} between the ZnCoS/NF_13 100, and the commercial NiFeCo/Ni mesh catalyst was not substantial, the synthesized catalyst still exhibited the lowest charge-transfer resistance. This suggests that ZnCoS/NF_13 100 has favourable interfacial charge-transfer properties, although its overall HER current density remains lower than that of the commercial NiFeCo/Ni mesh electrode.

For the oxygen evolution reaction (OER), the polarization curves in Figure 3(d) show that ZnCoS/NF_13 100 requires a lower potential to achieve benchmark current densities of 10 and 100 mA cm^{-2} compared with $NiFe_2O_4$/C and bare NF. The lower overpotential indicates a reduced energy requirement for water oxidation, highlighting the superior OER activity of ZnCoS/NF_13 100. The improved performance may be attributed to the presence of abundant active sites and enhanced electronic conductivity provided by the sulfide structure, which promotes the adsorption and conversion of OER intermediates such as *OH, *O, and *OOH. Meanwhile, bare NF requires the highest potential to reach the same current densities, reflecting sluggish OER kinetics.

Similarly, the OER Nyquist plots presented in Figure 3(e) reveal that ZnCoS/NF_13 100 exhibits the smallest semicircle diameter, followed by $NiFe_2O_4$/C and bare NF. The lower R_{ct} value of ZnCoS/NF_13 100 indicates faster charge transfer across the electrode–electrolyte interface, which facilitates the water oxidation and accelerates the OER process. The reduced resistance contributes to the lower overpotential observed in the LSV measurements. Therefore, the EIS results strongly support the superior OER activity demonstrated by ZnCoS/NF_13 100.

The impedance spectra were fitted using the equivalent circuit shown in Figure 3(f), consisting of the solution resistance (R_s), charge-transfer resistance (R_{ct}), and a constant phase element (CPE). The R_s value represents the resistance arising from the electrolyte and electrical contacts, while R_{ct} reflects the kinetic barrier associated with electron transfer during the electrochemical reaction. The incorporation of a CPE instead of an ideal capacitor accounts for the non-ideal capacitive behaviour resulting from surface roughness, porosity, and heterogeneity of the catalyst layer. The relatively low R_s values observed for all samples indicate minimal ohmic losses, suggesting that the differences in electrocatalytic performance are primarily governed by charge-transfer processes rather than solution resistance.

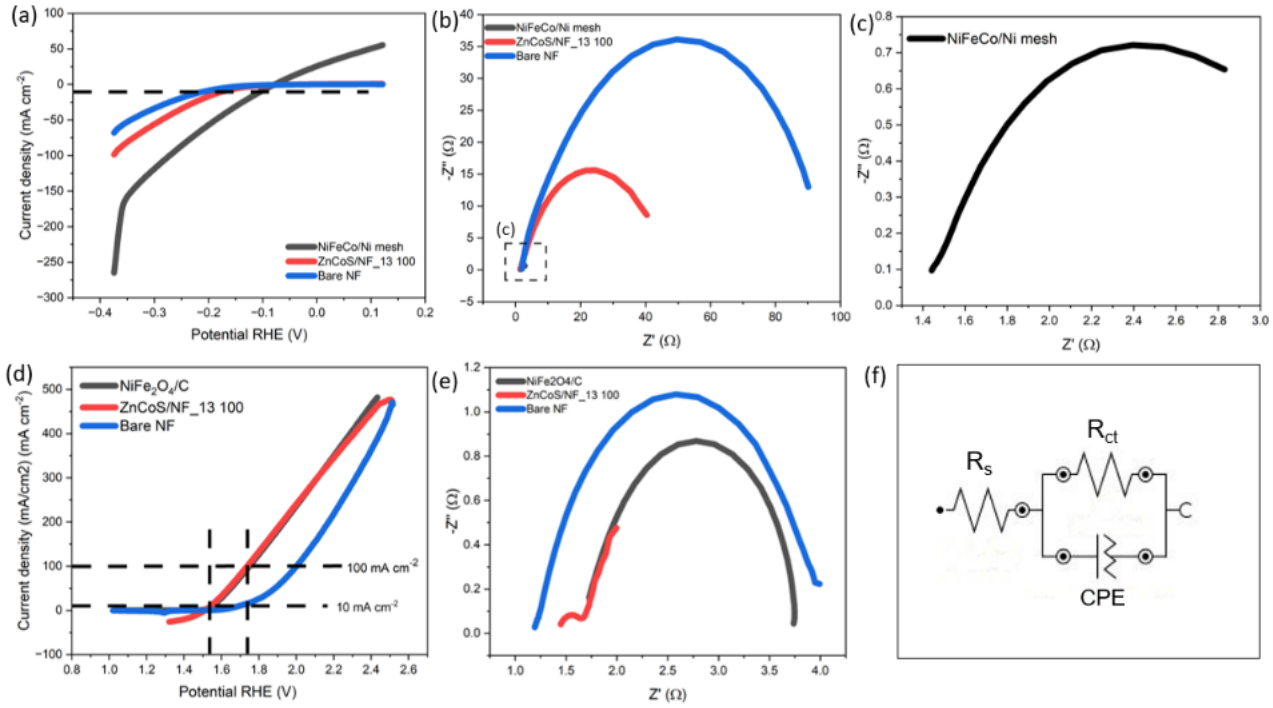


FIGURE 3. (a-c) Electrochemical testing for HER region where, (a) Linear sweep voltammetry (LSV), (b) electrochemical impedance spectroscopy (EIS), (c) enlargement of EIS in (b), specifically for NiFeCo/Ni mesh, ZnCoS/NF_13 100 and bare NF, (d-e) Electrochemical testing for OER region where, (d) LSV, (e) EIS for NiFe2O4/C, ZnCoS/NF_13 100 and bare NF, (f) equivalent circuit (Randle circuit) that use to fit each EIS curve.

TABLE 3. Overpotential and charge transfer resistance values for each sample according to HER and OER regions.

	HER			OER	
Sample	Overpotential (mV) at 10 mA/ cm^2	Charge transfer resistance, R_{ct} (Ω)	Sample	Overpotential (mV) at 10 mA/ cm^2	Charge transfer resistance, R_{ct} (Ω)
NiFeCo/Ni mesh	88.00	2.06	$NiFe_2O_4$/C	519.00	2.10
ZnCoS/NF_13 100	174.00	1.47	ZnCoS/NF_13 100	311.80	0.15
Bare NF	211.00	13.46	Bare NF	463.00	1.71

Overall, the LSV and EIS results consistently demonstrate that the NiFeCo/Ni mesh exhibits the most favourable HER performance, while ZnCoS/NF_13 100 shows the highest OER activity. The superior catalytic performances of these electrodes is closely associated with their lower charge-transfer resistance, enhanced electrical conductivity, and accelerated interfacial electron-transfer kinetics. These characteristics effectively reduce the activation energy of the electrochemical reactions, resulting in higher current densities and lower overpotentials during water-splitting processes.

CONCLUSIONS

In summary, we have successfully incorporated Zn^{2+} ion into CoS employing a two-step hydrothermal method with variations in the Zn doping concentrations and synthesis temperature. At a synthesis temperature of 100 °C, the formation of ZnCoS_13 results in a flower-like structure with abundant of interconnected nanoflakes morphology. In addition, XRD and HRTEM analyses confirm that the synthesized ZnCoS_13 100 exhibits the lowest cell volume, average crystallite size and crystallinity. These findings provide an insight into the structure–performance relationship, facilitating the development of catalysts that combine high accessibility of active sites with stable, conductive phases suitable for prolonged alkaline electrolysis. Therefore, the ZnCoS/NF_13 demonstrates superior structural and morphological properties, indicating its potential as an effective bifunctional catalyst for water electrolyser application. Further studies including electrochemical characterisations (CV, LSV, EIS, CA/CP, etc) and additional physical characterisations (XRF, XPS, TGA, etc) are required to determine the optimal catalyst for AEMWE systems.

ACKNOWLEDGEMENT

The current work was supported by the Malaysia Ministry of Higher Education (MOHE) through the Trans-disciplinary Research Grant Scheme (TRGS), grant code TRGS/1/2022/UKM/01/8/2.

DECLARATION OF COMPETING INTEREST

None.

REFERENCES

Arumugam, G., Mathan, S., Murugesan, V., Selvaraj, M., Albormani, O. & Rajendran, R. 2025. Enhanced electrochemical capacitive performance of zinc and cobalt metal-organic frameworks derived electrodes in redox additive electrolyte and their application in electrocatalytic water splitting. *Journal of Power Sources* 649: 237426.

Bakar, N. a. A., Salleh, N. A., Hamid, N. a. A., Abdullah, C. a. C., Rahiman, W., Basirun, W. J., Kheawhom, S. & Mohamad, A. A. 2022. The effect different of hydrochloric acid concentrations on the cleaning of Ni foam substrate: Structural and morphological studies. *Materials Today: Proceedings* 60: 1036-1041.

Bibi, K., Muqadas, S., Khan, M. M., Fatima, R., Sahar, F., Abbas Shah, S. I., Tighezza, A. M. & Khan, M. S. 2025. Improved water splitting performance for green hydrogen production using ZnCo2O4–CoFe2O4 composite Electrocatalyst. *International Journal of Hydrogen Energy* 106: 411-422.

Faid, A. Y., Barnett, A. O., Seland, F. & Sunde, S. 2021. NiCu mixed metal oxide catalyst for alkaline hydrogen evolution in anion exchange membrane water electrolysis. *Electrochimica Acta* 371: 137837.

Ferriday, T. B., Nuggehalli Sampathkumar, S., Middleton, P. H., Van Herle, J. & Kolhe, M. L. 2023. How Acid Washing Nickel Foam Substrates Improves the Efficiency of the Alkaline Hydrogen Evolution Reaction. *Energies* 16(5): 2083.

Krishnamachari, M., Kumar, M., Pandian, M. S., Vijayakumar, P. & Chang, J.-H. 2025. Self-assembly of binder-free 3D NiMoO4/ZnCo-LDH/NF core/shell architecture for efficient oxygen evolution reaction. *Fuel* 396: 135350.

Li, Y.-R., Jin, T., Pan, K.-M., Xu, L.-J., Li, H., Pan, S.-F., Ren, Y.-P. & Wei, S.-Z. 2025. In situ carbon-encapsulated CoS2/Zn0.76Co0.24S composite derived from intercalated CoZn-layered double hydroxide precursor for overall water splitting. *Tungsten* 7:

Morais, R. G., Rey-Raap, N., Figueiredo, J. L. & Pereira, M. F. R. 2023. Optimization of cobalt on CNT towards the oxygen evolution reaction and its synergy with iron (II) phthalocyanine as bifunctional oxygen electrocatalyst. *Catalysis Today* 418: 114057.

Park, S. H., Lee, S. H., Jeong, J.-Y., Jin, H., Ha, J. S., Lee, S. J., Kim, I. T., Kim, C., Kim, S., Bae, M., Lee, H., Choi, S. M., Yangdo, K. & Park, Y. S. 2023. Three-dimensional copper cobalt hydroxide electrode for anion exchange membrane water electrolyzer. *International Journal of Hydrogen Energy*:

Prabhakaran Shyma, A. & Sellappan, R. 2023. Synergistic performance of Zn2+ incorporated bimetallic Cobalt sulfide for the hydrogen evolution reaction in an alkaline medium. *Journal of Physics and Chemistry of Solids* 178: 111332.

Silva, J. O., Cartagena, S. & Calderón, J. A. 2023. Novel electrodeposited NiFeP/Zn bifunctional catalytic coating for alkaline water splitting. *Electrochimica Acta* 451: 142299.

Sugawara, Y., Sankar, S., Miyanishi, S., Illathvalappil, R., Gangadharan, P. K., Kuroki, H., Anilkumar, G. M. & Yamaguchi, T. 2023. Anion Exchange Membrane Water Electrolyzers: An Overview. *Journal of Chemical Engineering of Japan* 56(1): 2210195.

Viteri, J. P., Viteri, S., Alvarez-Vasco, C. & Henao, F. 2023. A systematic review on green hydrogen for off-grid communities –technologies, advantages, and limitations. *International Journal of Hydrogen Energy* 48(52): 19751-19771.

Wang, Z., Wang, Z., Wang, J., Shi, H., Wang, C., Fan, Y., Bai, Z., Zhu, C. & Yan, X. 2023. Ni, Zn Co-doping ZIF-67-derived electrocatalyst based on CNT film for efficient overall water splitting. *International Journal of Hydrogen Energy*:

Wu, Q., Gu, J., Wang, J., Liu, N. & Chaemchuen, S. 2023. Impact in rational synthesis Co-ZIF templates for derived the structural Co@NC catalysis for high efficient hydrogen and oxygen evolution reactions. *International Journal of Hydrogen Energy* 48(7): 2663-2676.